The role of conductive heat losses on the formation of isolated flame cells in Hele-Shaw chambers

Daniel Martínez-Ruiz[a,*], Fernando Veiga-López[b], Daniel Fernández-Galisteo[c], Vadim N. Kurdyumov[c], Mario Sánchez-Sanz[b]

[a] *E.T.S.I.A.E., Universidad Politécnica de Madrid, Plaza del Cardenal Cisneros 3, Madrid, Spain*
[b] *Fluid Mechanics Group, Universidad Carlos III de Madrid, Avda. de la Universidad 30, Leganés, Spain*
[c] *Department of Energy, CIEMAT, Avda. Complutense 40, Madrid, Spain*

Abstract

The propagation of low-Lewis-number premixed flames is analyzed in a partially confined Hele–Shaw chamber formed by two parallel plates separated a distance h apart. An asymptotic-numerical study can be performed for small gaps compared to the flame thickness δ_T. In this narrow-channel limit, the problem formulation simplifies to a quasi-2D description in which the velocity field is controlled by dominant viscous effects. After accounting for conductive heat losses through the plates in our formulation, we found that the reaction front breaks into one or several isolated flame cells where the temperature is large enough to sustain the reaction, both in absence and in presence of buoyancy effects. Under these near-limit conditions, the isolated flame cells either travel steadily or undergo a slow random walk over the chamber in which the reacting front splits successively to form a tree-like pathway, burning only a small fraction of the fuel before reaching the end of the chamber. The production of quasi-2D circular or comet-like flames under specific favorable conditions is demonstrated in this paper, with convection, conductive heat losses and differential diffusion playing an essential role in the formation of the isolated one and two-headed flame cells.

Keywords: low-Lewis number, Hele–Shaw chamber, conductive heat losses, flame circles, comet flames.

1. Introduction

The study of flames in confined geometries is relevant to the development of small-scale combustors and the design of internal combustion engines, as well as to provide further insight on safety issues and undesired propagation of confined reactions in small channels, gaps and tubes. In turn, it is widely-accepted that micro-combustion devices have benefited from the study of numerous performance issues such as flame instabilities [1, 2], thermoacoustic coupling [3], flame extinction and quenching [4], amongst others. The study of the

*Corresponding author
Email address: daniel.mruiz@upm.es (Daniel Martínez-Ruiz)

propagation of premixed-gas flames in narrow chambers is key to understand most of these phenomena, which are typically enhanced by the geometrical restraint of the flow. Experimental, theoretical and numerical efforts have been instrumental in providing insight on the flame shape [5, 6], the propagation rate [7–9] and the flame stability under various conditions and regimes [5, 10–14].

Furthermore, safety issues related to fuel leakage that may lead to fire and explosion accidents motivate the appearance of new fundamental studies. Besides the most destructive events, such as detonations and material combustion, one of the challenges is to detect and control very lean and slow-burning combustion fronts that can deliver undesired hot spots into flammable regions. These kernels may be able to travel in favor or against gravity under different circumstances. The description of this variety of new regimes in confined lean-burning processes is imperative to design updated prevention strategies.

Specifically, combustion of hydrogen has captured the scientific community's interest, including studies on lean mixtures, near-limit conditions and differential-diffusion effects because of their practical [15] and scientific interest [16, 17]. Droznov and Zel'dovich [18] in 1943 and Zel'dovich [19] in 1944 predicted theoretically the existence of non-propagating flame balls in a quiescent atmosphere, later confirmed by Ronney in microgravity experiments [20]. Following the suggestions made by Zel'dovich, Buckmaster et al. [21–23] demonstrated that flame balls can be stabilized when radiation heat losses offset the excess of heat accumulated near the reaction region. Later, Grcar [24] found a stable solution in non-buoyant computations in which the flames travel at constant velocity adopting hemispherical shapes and in the absence of radiative losses. Recently, under standard gravity conditions, Zhou et al. [25] have experimentally found a combustion regime in which hydrogen burns forming an array of unstable ball-like flames.

The analytical solutions proposed by [21–23] are valid for spherical flame balls. However, it is not possible to obtain a physically-acceptable mathematical solution of a steady two-dimensional circular flame. To prove this point, first consider a planar quiescent reactive-diffusive system in which the fuel is consumed in a circular flame front to release an amount of heat Q'. The corresponding conservation equations for energy and deficient species Y' written in radial cylindrical coordinates yield

$$\frac{1}{r}\frac{d}{dr}\left(r\lambda\frac{dT}{dr}\right)+Q'\omega-\hat{b}=0, \qquad \frac{1}{r}\frac{d}{dr}\left(r\rho'\mathcal{D}'\frac{dY'}{dr}\right)-\omega=0, \tag{1}$$

with T the gas temperature, λ the thermal conductivity, $\mathcal{D}'$ the species diffusivity, ω the reaction rate and $\hat{b}$ a generic heat-loss function. Given that the flame surface is located at $r=r_f$, the system of equations (1) must be integrated with boundary conditions $T-T_f=Y=0$ at $r=r_f$ and $T-T_u=Y-1=0$ at $r\to\infty$, with T_u and T_f the temperature of the unburnt and burnt gases, respectively. Out of the thin flame surface $r\to\infty$, the reaction vanishes $\omega=0$ and both equations can be easily integrated. Once the heat-loss function $\hat{b}>0$ is known, we can easily integrate the first equation in (1) to obtain a temperature profile that decays smoothly towards T_u. However, regardless of $\hat{b}$, the mass fraction profile is always of the form $Y=C_1\ln r+C_2$, with C_1 and C_2 representing the integration constants

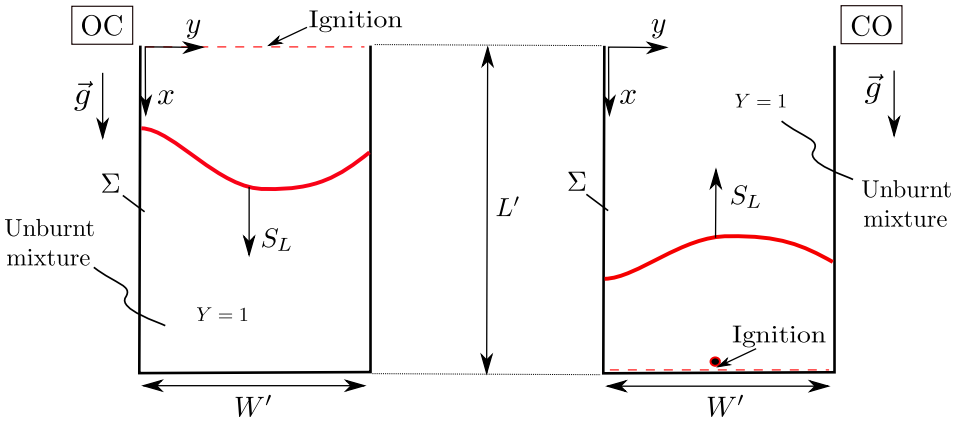

Figure 1: Sketch of the Hele–Shaw chamber of dimensions $L' \times W'$ in the open-closed OC (left) and closed-open CO (right) configurations, where $\vec{g}$ is the general gravity acceleration vector and S_T the overall flame propagation velocity.

whose value cannot be chosen to simultaneously satisfy the boundary conditions both at infinity and at $r = r_f$.

In spite of this analytical discussion and encouraged by the results of Grcar [24], a quasi-2D methodology is used here to explore the practicability of stable comet and circle-like traveling flames in low-Lewis number reactive mixtures. Their formation is studied in a Hele–Shaw chamber formed by two parallel plates that are separated a small distance apart, sketched in Fig. 1 under two different configurations. In the limit considered in this work, in which the separation between plates is asymptotically small compared to any other length scale of the problem, the flame dynamics can be studied using a quasi-2D formulation that preserves the physics of the process and keeps the computational cost within limits [12]. Initially, the volume between the plates Σ is filled with unburnt reactants, which are progressively consumed after ignition at $t = 0$. The lateral walls of the chamber are closed except for one side which is configured as a venting section placed either at the ignition or at the opposite end of the domain. Even though partial confinement is responsible for the first order dynamics of the flame, conductive heat losses are key in the conformation of the flame morphology. As we show in this work, non-adiabatic plates favor the transition from a continuous flame front to a set of isolated flame cells. The dynamic of these flame cells will be explored in subsequent sections of the paper in terms of the different parameters involved in the problem.

The paper is structured as follows. In section 2 we explain the separation of the physical scales of the problem as a first step to develop the mathematical formulation that describes the propagation of premixed flames in narrow channels including heat losses. The following sections 3 and 4 summarize the results and include the effect of heat losses in several Hele–Shaw configurations with and without the effect of gravity. Details on circular and comet-like flames stabilized by wall heat losses are shown in section 5. Finally, concluding remarks are

given in section 6. The finite-element method employed here to integrate the simulations is later presented in Appendix A, together with its validation and specified numerical details.

2. Mathematical formulation

The problem addressed here first considers a fresh homogeneous mixture of reactants of density ρ_u and temperature T_u. These gases are confined between two parallel plates of dimensions $L' \times W'$ separated a distance h apart. Upon an ignition event, the overall propagation rate of the flame front S_T is determined by the kinetics of the reaction and the induced flame wrinkling. A simplified one-step irreversible scheme is proposed to model the chemical reaction,

$$\nu_F \cdot \text{Fuel} + \nu_\text{O} \cdot \text{Oxidizer} \rightarrow \text{Products} + Q', \tag{2}$$

where Q' is the heat produced by the reaction and ν_i are the stoichiometric coefficients. In the limit of very lean flames studied here, the chemical reaction rate can be written in the Arrhenius form

$$\omega = \mathcal{B}(\rho')^2 \frac{Y'}{\mathcal{M}} \exp\left(-\frac{E}{\mathcal{R}T}\right), \tag{3}$$

where E is the global activation energy required to trigger the reaction, $\mathcal{R}$ is the universal gas constant, $\mathcal{B}$ is the frequency factor, Y' is the mass fraction of the deficient reactant and $\mathcal{M}$ its molecular mass.

2.1. Scales and governing equations

Changes in the fluid properties along the in-plane coordinates (x, y) are produced across distances of the order of the flame thickness $\delta_T = \mathcal{D}_{T_u}/S_L$, with $\mathcal{D}_{T_u}$ the thermal diffusivity of the fresh gas mixture and S_L the burning velocity of the planar adiabatic flame. Therefore, we scale the problem using δ_T as the the characteristic length to define the non-dimensional coordinates $x = x'/\delta_T$ and $y = y'/\delta_T$, with the transverse coordinate $z = z'/h$ scaled with the gap size h. S_L is used to define the dimensionless gas velocity variables $u_x = u'_x/S_L$ and $u_y = u'_y/S_L$. The appropriate scale of the transverse velocity $u_z = u'_z/(aS_L)$ is determined by an order-of-magnitude analysis of the continuity equation, with $a = h/\delta_T$. Using the aforementioned magnitudes, the dimensionless time is defined as $t = t'/(\delta_T/S_L)$.

The state variables satisfy the ideal gas equation $p' = \rho' R_g T$, with R_g the gas constant of the mixture. Therefore, pressure is scaled with the initial value $\rho_u R_g T_u$. It must be noted that, thermodynamic pressure $P'(t)$ is differentiated from the hydrodynamic variation $p' - P'(t)$. Thus, the ideal gas equation in its dimensionless form reads

$$\rho(1 + q\theta) = P(t) + \gamma \left(\frac{M}{a}\right)^2 p, \tag{4}$$

where the dimensionless variables are $P(t) = P'(t)/(\rho_u R_g T_u)$ the thermodynamic pressure, $p = [p' - P'(t)]/[\rho_u S_L^2/a^2]$ the hydrodynamic pressure variation, $\rho = \rho'/\rho_u$ the mixture

density and $\theta = (T - T_u)/(T_a - T_u)$ the temperature. Moreover, $q = (T_a - T_u)/T_u$ is the dimensionless heat of reaction, with the adiabatic temperature of the flame defined as

$$T_a = T_u + \frac{Y_u Q'}{c_p \nu_F \mathcal{M}} = T_u(1+q), \tag{5}$$

and ν_F the stoichiometric coefficient of the limiting reactant. Using the dimensionless variables defined above, the continuity and momentum equations can be written as,

$$\frac{\partial \rho}{\partial t} + \frac{\partial(\rho u_x)}{\partial x} + \frac{\partial(\rho u_y)}{\partial y} + \frac{\partial(\rho u_z)}{\partial z} = 0 \tag{6}$$

$$\rho\left[\frac{\partial u_x}{\partial t} + u_x\frac{\partial u_x}{\partial x} + u_y\frac{\partial u_x}{\partial y} + u_z\frac{\partial u_x}{\partial z}\right] = -\frac{1}{a^2}\frac{\partial p}{\partial x} + Pr\left[\frac{\partial \tau_{xx}}{\partial x} + \frac{\partial \tau_{xy}}{\partial y} + \frac{1}{a}\frac{\partial \tau_{xz}}{\partial z}\right] \pm \frac{\rho G}{a^2}, \tag{7}$$

$$\rho\left[\frac{\partial u_y}{\partial t} + u_x\frac{\partial u_y}{\partial x} + u_y\frac{\partial u_y}{\partial y} + u_z\frac{\partial u_y}{\partial z}\right] = -\frac{1}{a^2}\frac{\partial p}{\partial y} + Pr\left[\frac{\partial \tau_{yx}}{\partial x} + \frac{\partial \tau_{yy}}{\partial y} + \frac{1}{a}\frac{\partial \tau_{yz}}{\partial z}\right], \tag{8}$$

$$\rho\left[\frac{\partial u_z}{\partial t} + u_x\frac{\partial u_z}{\partial x} + u_y\frac{\partial u_z}{\partial y} + u_z\frac{\partial u_z}{\partial z}\right] = -\frac{1}{a^4}\frac{\partial p}{\partial z} + \frac{Pr}{a}\left[\frac{\partial \tau_{zx}}{\partial x} + \frac{\partial \tau_{zy}}{\partial y} + \frac{1}{a}\frac{\partial \tau_{zz}}{\partial z}\right], \tag{9}$$

where the Prandtl number is $Pr = \mu_u/(\rho_u \mathcal{D}_{T_u}) = 0.7$ and $G = g\sin(\alpha)\delta_T a^2/S_L^2$ is the gravity term included in the longitudinal direction to act against or in favor of the global flame propagation, with α the angle formed by the gravity vector and the normal to the Hele–Shaw cell $\vec{e}_z$. The viscous terms are written as

$$\begin{aligned}
\tau_{xx} &= \mu\left(2\frac{\partial u_x}{\partial x} - \frac{2}{3}\nabla\cdot\bar{u}\right), \qquad \tau_{xy} = \tau_{yx} = \mu\left(\frac{\partial u_x}{\partial y} + \frac{\partial u_y}{\partial x}\right),\\
\tau_{yy} &= \mu\left(2\frac{\partial u_y}{\partial y} - \frac{2}{3}\nabla\cdot\bar{u}\right), \qquad \tau_{yz} = \tau_{zy} = \mu\left(\frac{1}{a}\frac{\partial u_y}{\partial z} + a\frac{\partial u_z}{\partial y}\right),\\
\tau_{zz} &= \mu\left(2\frac{\partial u_z}{\partial z} - \frac{2}{3}\nabla\cdot\bar{u}\right), \qquad \tau_{zx} = \tau_{xz} = \mu\left(\frac{1}{a}\frac{\partial u_x}{\partial z} + a\frac{\partial u_z}{\partial x}\right),
\end{aligned}$$

with the viscous coefficient $\mu = \mu'/\mu_u$. The conservation equation for the mass fraction of the deficient species $Y = Y'/Y_u$ yields

$$\begin{aligned}
\rho\left[\frac{\partial Y}{\partial t} + u_x\frac{\partial Y}{\partial x} + u_y\frac{\partial Y}{\partial y} + u_z\frac{\partial Y}{\partial z}\right] &= \\
= \frac{1}{Le}\left[\frac{\partial}{\partial x}\left(\rho\mathcal{D}\frac{\partial Y}{\partial x}\right)\right. &+ \left.\frac{\partial}{\partial y}\left(\rho\mathcal{D}\frac{\partial Y}{\partial y}\right) + \frac{1}{a^2}\frac{\partial}{\partial z}\left(\rho\mathcal{D}\frac{\partial Y}{\partial z}\right)\right] - \Omega,
\end{aligned} \tag{10}$$

with $\mathcal{D} = \mathcal{D}'/\mathcal{D}_u$ the species mass diffusivity coefficient, $Le = \mathcal{D}_{T_u}/\mathcal{D}_u$ the Lewis number, and $\Omega = (\omega\nu\mathcal{M}\mathcal{D}_{T_u})/(\rho_u S_L^2 Y_u)$ the dimensionless reaction rate. The energy equation in terms of θ is reduced to

$$\begin{aligned}
\rho\left[\frac{\partial \theta}{\partial t} + u_x\frac{\partial \theta}{\partial x} + u_y\frac{\partial \theta}{\partial y} + u_z\frac{\partial \theta}{\partial z}\right] &= \frac{\gamma-1}{q}\left[\frac{1}{\gamma}\frac{\partial P}{\partial t} + \left(\frac{M}{a}\right)^2\left(\Phi_v Pr + \frac{\partial p}{\partial t} + u_x\frac{\partial p}{\partial x} + u_y\frac{\partial p}{\partial y} + u_z\frac{\partial p}{\partial z}\right)\right] +\\
+\frac{\partial}{\partial x}\left(\rho\mathcal{D}_T\frac{\partial \theta}{\partial x}\right) &+ \frac{\partial}{\partial y}\left(\rho\mathcal{D}_T\frac{\partial \theta}{\partial y}\right) + \frac{1}{a^2}\frac{\partial}{\partial z}\left(\rho\mathcal{D}_T\frac{\partial \theta}{\partial z}\right) + \Omega,
\end{aligned} \tag{11}$$

where $\mathcal{D}_T = \mathcal{D}'_T/\mathcal{D}_{T_u}$ is the nondimensional thermal diffusivity, $\gamma = c_p/c_v$ is the adiabatic index and Φ_v is the viscous dissipation,

$$\Phi_v = a^2\mu\left\{2\left[\left(\frac{\partial u_x}{\partial x}\right)^2+\left(\frac{\partial u_y}{\partial y}\right)^2+\left(\frac{\partial u_z}{\partial z}\right)^2\right]+\left[\frac{\partial u_y}{\partial x}+\frac{\partial u_x}{\partial y}\right]^2+\right.$$
$$\left.+\left[\frac{1}{a}\frac{\partial u_y}{\partial z}+a\frac{\partial u_z}{\partial y}\right]^2+\left[a\frac{\partial u_z}{\partial x}+\frac{1}{a}\frac{\partial u_x}{\partial z}\right]^2-\frac{2}{3}\left[\frac{\partial u_x}{\partial x}+\frac{\partial u_y}{\partial y}+\frac{\partial u_z}{\partial z}\right]^2\right\}. \tag{12}$$

In addition, the dimensionless diffusive transport coefficients follow a power law with temperature in the form $\mu = \rho\mathcal{D}_T = \rho\mathcal{D} = (1+q\theta)^\sigma$. Finally, the dimensionless reaction rate is defined by the expression

$$\Omega = \rho^2\beta^2(1+q)^{2-\sigma}\frac{Y}{2s_L^2 Le}\exp\left(\frac{\beta(\theta-1)}{1+\frac{q}{q+1}(\theta-1)}\right), \tag{13}$$

with the Zel'dovich number defined as $\beta = E(T_a - T_u)/(\mathcal{R}T_a^2)$. The factor $s_L = (S_L)/(S_L)_{asp} = 1.05$ is the eigenvalue of the planar adiabatic problem [5], where the propagation velocity S_L for finite β is compared with the propagation velocity for infinitely-large activation energy $(S_L)_{asp}$.

To account for the effect of conductive heat losses on the propagation of the flame, the heat equation must be solved in the solid plates that bound the channel. Considering that the temperature on the external surface of the plates is maintained at T_u and that the plates thickness is h_w, the temperature in the solid walls $\theta_w = (T_w - T_u)/(T_a - T_u)$ can be obtained by integrating the non-dimensional heat equation

$$-\frac{\rho_w c_w}{\rho_u c_p}\frac{\partial\theta_w}{\partial t}+\frac{\partial}{\partial x}\left(\frac{\lambda_w}{\lambda_u}\frac{\partial\theta_w}{\partial x}\right)+\frac{\partial}{\partial y}\left(\frac{\lambda_w}{\lambda_u}\frac{\partial\theta_w}{\partial y}\right)+\frac{1}{a^2}\frac{\partial}{\partial z}\left(\frac{\lambda_w}{\lambda_u}\frac{\partial\theta_w}{\partial z}\right)=0, \tag{14}$$

where ρ_w, λ_w and c_w are the density, the thermal conductivity and the heat capacity of the solid plates, respectively, and λ_u is the thermal conductivity of the fresh gas mixture. For convenience, we only define here the boundary conditions in z direction required to solve the system of equations (6)-(14), where

$$u_x = u_y = u_z = \frac{\partial Y}{\partial z} = 0, \qquad \theta_w = \theta, \qquad \frac{\partial\theta}{\partial z} = a^2\frac{b}{2\mu}\frac{h_w}{h}\frac{\partial\theta_w}{\partial z} \tag{15}$$

along the inner surface of the solid plates $z = 0$ and $z = 1$ and $\theta_w = 0$ on the outer surface of the solid plates $z = -h_w/h$ and $z = 1 + h_w/h$. The order-unity heat-loss parameter

$$b = \frac{2}{a^2}\frac{h}{h_w}\frac{\lambda_w}{\lambda_u} \geq 0, \tag{16}$$

naturally arises to quantify the rate of heat flux across the walls. In addition, symmetry is imposed at the midplane of the channel $z = 1/2$,

$$v = \frac{\partial u}{\partial z} = \frac{\partial Y}{\partial z} = \frac{\partial\theta}{\partial z} = 0. \tag{17}$$

2.2. Quasi-2D limit in semi-confined geometries

The three-dimensional problem presented above can be simplified in the limit of low-Mach propagation $(M/a) \ll 1$ and very narrow channels $a = h/\delta_T \ll 1$ to a much simpler quasi-2D problem. The characteristic Reynolds number $Re = \rho_u S_L h/\mu_u = a/Pr \ll 1$ is small. In the cases studied here, hydrodynamic pressure variations $p'(x, y, z; t) \sim \rho_u S_L^2/(h/\delta_T)^2$ are much smaller than the thermodynamic pressure $P'(t) \sim \rho_u R_g T_u$, yielding $p'/P' \sim (M/a)^2 \ll 1$ and neglecting $\partial P/\partial t$ in (11). The simplified equation of state takes its quasi-isobaric form,

$$\rho(1 + q\theta) = 1, \tag{18}$$

with the vessel open to the atmosphere at one end. In this narrow-channel limit, the flow field variables $\Psi = \{\theta_w, \theta, Y, p\}$, are accordingly expanded as [26]

$$\Psi = \Psi_0 + a^2\Psi_1 + \mathcal{O}(a^4)\cdots \tag{19}$$

Introducing this perturbed expansion in (10), (11) and (14), we obtain to leading order

$$\frac{\partial}{\partial z}\left(\rho_0 \mathcal{D}_T \frac{\partial \theta_0}{\partial z}\right) = \frac{\partial}{\partial z}\left(\rho_0 \mathcal{D} \frac{\partial Y_0}{\partial z}\right) = \frac{\partial}{\partial z}\left(\frac{\lambda_w}{\lambda_u}\frac{\partial \theta_{w0}}{\partial z}\right) = 0 \tag{20}$$

which yields, after imposing the boundary conditions (15) and (17), constant profiles of species and gas temperature in the transverse coordinate $\theta_0 = \theta_0(x, y; t)$, $Y_0 = Y_0(x, y; t)$ and a linear profile for the upper $\theta_{w0} = \theta_0[1 + (1 - z)h/h_w]$ and lower $\theta_{w0} = \theta_0(1 + zh/h_w)$ wall temperatures.

In turn, the momentum equation in the z direction simplifies to $\partial p_0/\partial z = 0$ to give $p_0 = p_0(x, y; t)$. The separation between the plates is small enough to make the viscous terms dominant in (7) and (8) with the velocity profiles instantly developing as a Poiseuille flow $u_{0_x} = 6z(1 - z)U_x$ and $u_{0_y} = 6z(1 - z)U_y$, with

$$U_x = -\frac{1}{12\mu Pr}\left(\frac{\partial p_0}{\partial x} \pm \rho_0 G\right) \quad \text{and} \quad U_y = -\frac{1}{12\mu Pr}\frac{\partial p_0}{\partial y} \tag{21}$$

obtained after imposing the non-slip boundary conditions (15). The equations to account for the first-order corrections ($\sim \mathcal{O}(a^2)$) of temperature θ_1, mass fraction Y_1 and pressure p_1 can be easily obtained by introducing the expanded variables (19) in the continuity (6), species (10) and energy (11) equations. An average contribution of the transverse variations is therefore included by integrating the resulting expressions in the z direction and imposing the wall-boundary conditions at the plates

$$\text{at } z = 1, \quad Y_1 = 0, \quad \frac{\partial \theta_1}{\partial z} = -\frac{b}{2\mu}\theta_0, \tag{22}$$

$$\text{at } z = 0, \quad Y_1 = 0, \quad \frac{\partial \theta_1}{\partial z} = \frac{b}{2\mu}\theta_0. \tag{23}$$

As a result, the equations for the first-order terms θ_0, Y_0, p_0, constant in z, yield

$$\frac{\partial \rho_0}{\partial t} + \frac{\partial}{\partial x}\left(\rho_0 U_x\right) + \frac{\partial}{\partial y}\left(\rho_0 U_y\right) = 0, \tag{24}$$

$$\rho_0 \frac{\partial \theta_0}{\partial t} + \rho_0 U_x \frac{\partial \theta_0}{\partial x} + \rho_0 U_y \frac{\partial \theta_0}{\partial y} = \nabla \cdot \left(\rho_0 \mathcal{D}_T \nabla \theta_0\right) + \Omega - b\theta_0, \tag{25}$$

$$\rho_0 \frac{\partial Y_0}{\partial t} + \rho_0 U_x \frac{\partial Y_0}{\partial x} + \rho_0 U_y \frac{\partial Y_0}{\partial y} = \frac{1}{Le} \nabla \cdot \left(\rho_0 \mathcal{D} \nabla Y_0\right) - \Omega, \tag{26}$$

where the operator ∇ is defined in the (x, y) plane. Finally, combining Eqs. (18), (24), (25), and making use of the Poiseuille description (21), we can develop an expression for the spatial variations of pressure,

$$\frac{1}{12Pr}\nabla^2 p_0 = q\mu\left[\nabla \cdot \left(\mu \nabla \theta_0\right) + \Omega - b\theta_0\right] + \frac{1}{12Pr}\left[\nabla\mu\nabla p_0 \pm \frac{\partial \rho_0}{\partial x} G \mp \rho_0 G \frac{\partial \mu}{\partial x}\right]. \tag{27}$$

The complete formulation presented here accounts for the thermal expansion of the burnt gases, buoyancy, temperature-dependent diffusion coefficients, thermo-diffusive effects, conductive heat losses at the walls and dynamic pressure variations in the premixed-flame combustion problem in open chambers. Therefore, it allows the analysis through numerical simulations of separated effects, such as the Rayleigh-Taylor, Darrieus–Landau, Saffman–Taylor and cellular instabilities, on flame dynamics, local quenching, flame wrinkling, and change of the propagation speed.

2.3. Boundary and initial conditions

The problem to be solved, defined by the system (18), (21) and (25)-(27) requires of specific boundary conditions in the 2D plane. We consider, at $y = 0$, $y = W$ and $x = L$ adiabatic and non-permeable walls

$$\frac{\partial p_0}{\partial n} = 0, \quad \frac{\partial Y_0}{\partial n} = 0, \quad \frac{\partial \theta_0}{\partial n} = 0, \tag{28}$$

with n representing the normal direction to each of the boundaries. The boundary at $x = 0$ is left open to the ambient $p_0 = 0$, allowing a net flux of mass, species and temperature out of the chamber, and the subscript 0 is dropped for simplicity from now on.

The ignition mechanism strongly influences the evolution of the reaction propagation by defining the state of the mixture just after the energy deposition. The initial condition at $t = 0$ is an unburnt mixture, $Y = 1$, at rest, $p = 0$, and a temperature field that decays exponentially with the distance from the ignition line placed at x_0. The latter is perturbed as a sinusoid of small amplitude $A = 0.01$ in the y direction,

$$\theta = \theta_i \left[1 + A \sin\left(2\pi k_i \frac{y}{W}\right)\right] \exp\left\{-\frac{|x - x_0|}{r_0}\right\}, \tag{29}$$

with $\theta_i = 2.5$ and $r_0 = 1$ the dimensionless temperature and size of the ignition regions respectively. The parameter k_i is introduced to incorporate a perturbation wavenumber in

Parameter	**Symbol**	**Value**
Gravity parameter	$G = g\sin(\alpha)\delta_T a^2/S_L^2$	$-10 < G < 10$
Heat of reaction	$q = (T_a - T_u)/T_u$	5
Heat capacity ratio	$\gamma = c_p/c_v$	1.4
Heat losses	$b = 2(h/h_w)(\lambda_w/\lambda_u)/a^2$	$0 < b < 2.5$
HS chamber width	W	30
HS chamber length	L	100
Ignition Temperature	θ_i	2.5
Ignition size	r_0	1
Ignition location	x_0/L	0.01 or 0.99
Ignition wavenumber	k_i	2
Lewis number	$Le = \mathcal{D}_{T_u}/\mathcal{D}_u$	0.3
Prandtl number	$Pr = \mu_u/(\rho_u \mathcal{D}_{T_u})$	0.7
Planar velocity ratio	$s_L = S_L/(S_L)_{asp}$	1.05
Zel'dovich Number	$\beta = E(T_a - T_u)/(R_g T_a^2)$	10
Transport power law	σ	0

Table 1: Value of the dimensionless physical parameters used in the computations below.

the wrinkling and propagation of the flame. Moreover, the initial condition (29) allows for calculation of two different configurations, as sketched in Fig. 1. When $x_0 = 0.01L$, the ignition end remains open and the flame propagates toward the closed end of the Hele–Shaw chamber, progressively building up pressure that opposes to the thermally-induced flow (open-closed configuration, OC). On the other hand, imposing $x_0 = 0.99L$, ignition takes place at the closed end and the flame propagates towards the open end, which enhances the flame velocity as a consequence of the expansion of burnt gases acting against the back wall (closed-open configuration, CO). Bearing in mind the objective of isolating certain physical processes, such as the ones caused by heat losses, the numerical simulations are first presented here with $\sigma = 0$ for the temperature power law of the diffusion coefficients. The values of the following parameters, $k_i = 2$, $\gamma = 1.4$, $Pr = 0.7$, $q = 5$, $Le = 0.3$, $L = 100$ and $W = 30$ are kept constant hereafter if not specified otherwise.

The numerical solutions presented below are provided by the integration of the system of equations using an in-house finite element code with adaptive triangulated grid that uses piece-wise quadratic functions for θ_0, Y_0 and linear piece-wise polynomials for pressure p_0 in order to satisfy the inf-sup (or Babuska–Brezzi) condition [27]. A second-order backward difference formula (BDF scheme) is applied for time discretization. Additional details on the numerical method, the grid refinement procedure and the validation of the code are given in the Appendix.

3. Heat-loss effects in non-buoyant flames

This section explores the effects of increasing conductive heat losses at the channel walls on the propagation of highly diffusive fuel flames and the transition from a continuous front into a set of isolated circle or comet-like flames. In order to isolate other physical contributions, we first consider premixed flames not affected by gravity ($G = 0$) in this section. Different ignition locations are proposed, at the open or closed ends, to respectively account for the pressure effect of confined fresh or burnt gases on the stabilization of the circle and comet-like flame regimes. It can be directly observed that the flame front is rapidly wrinkled in all cases due to Darrieus–Landau and thermo-diffusive instabilities. The former is inherent to density changes while the latter is promoted due to the unequal values of thermal to molecular diffusion coefficients (low-Lewis number). However, it must be noted that values of $Le \gtrsim 1$ can overcome the flame wrinkling and stabilize the reactive front. An equidiffusional case ($Le = 1$) is considered to demonstrate that the isolated weak cells rely on highly-diffusive mixtures.

3.1. Open-closed propagation

Premixed flames advancing towards a closed end produce a confinement effect on the fresh reactants that progressively rises the pressure ahead of the flame front. For this case, the temperature profile is initialized with a sinusoidal perturbation at $x_0 = 0.01L$ that is naturally amplified during the initial time steps. The results for increasing values of the heat-loss parameter b are shown in Fig. 2. Coloured isocontours depict the distribution of temperature and the arrows represent the flow field at the last time instant shown in each case ($t = 4.5$ for $b = 0$, $t = 5.0$ for $b = 0.5$, $t = 5.0$ for $b = 0.75$ and $t = 6.5$ for $b = 1$). Likewise, dim solid lines are used to represent the reaction rate isocontours for intermediate times to generate a visual representation of the flame front evolution. In the absence of heat losses ($b = 0$), the flame acquires the classical cellular structure induced by the thermo-diffusive instabilities with an overall flame front that propagates along the chamber. Well-defined cells grow together in amplitude and divide the front by extinction of the receding troughs, as observed previously in [28]. At those points, fresh reactants crossing the flame towards the high-temperature region of the domain can be found, generating localized tails of lower temperature. In addition, the cellular instability generates a rapid loss of symmetry in the y axis, which unbalances the pressure build-up in the confined region. Transverse pressure gradients displace laterally the unburnt mixture and generate a preferential venting corridor on one side of the chamber that makes possible the leakage of unburnt reactants through the open end out of the computational domain. Additionally, the higher the heat-loss parameter the lower the maximum temperatures reached in the domain, thus reducing the mean propagation velocity. Therefore, the size of the venting channel increases with b, as the flame becomes weaker and more easily blown backwards by the self induced overpressure.

The cellular character of the flame is promoted by division of the reaction front via the extinguished cusps when the heat loss parameter is increased. For $b = 0.5$ in Fig. 2 we can observe an increase of the number of cells separated from each other by cold reacts. Further increase of the heat loss, with $b = 0.75$, induces the formation of elongated comet-like flame

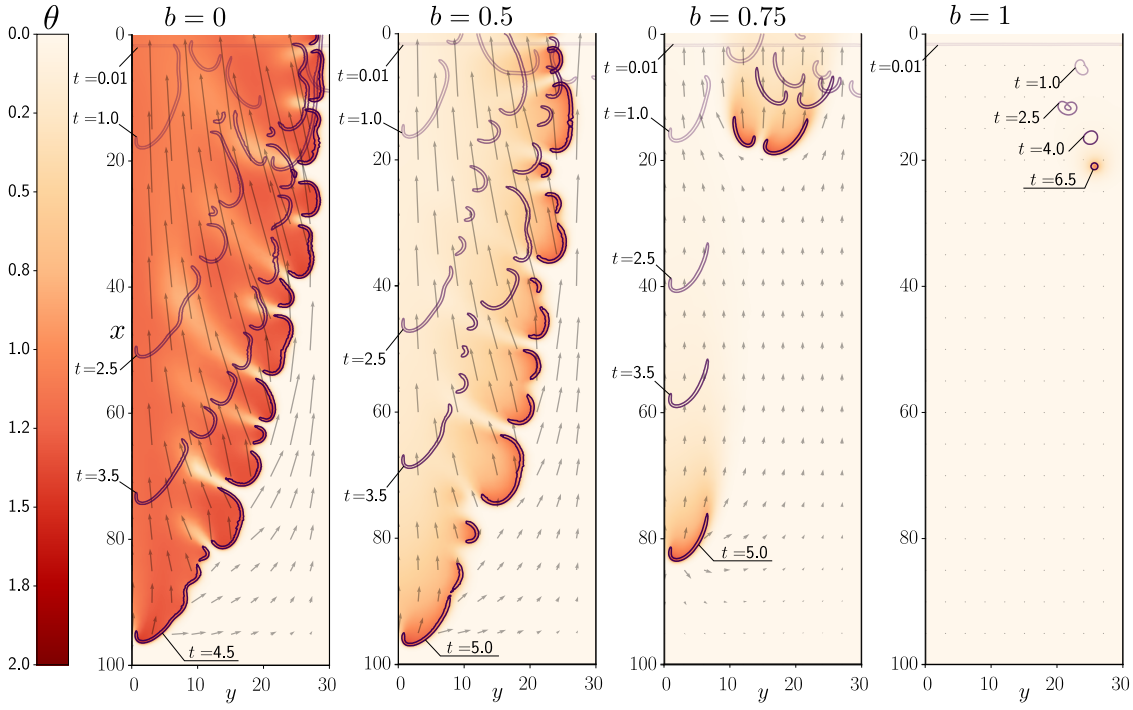

Figure 2: Flame front evolution in non-buoyant OC propagation at different times for increasing values of the heat-loss parameter b. The colormap represents the nondimensional temperature profile. The arrow field shows the flow direction and intensity, both at the last instant depicted in each panel.

structures, somehow similar to the propagating hemispherical flames found by Grcar [24] in his adiabatic 2D calculations and by Kagan et al. [29] in their non-adiabatic 3D simulations. Here, the reacting fronts are stabilized by the combined effects of the surrounding convective flow, high diffusion of unburnt species behind the flame tails and conductive heat losses. As shown later in Fig. 4, only half of the fuel is burned before the flame reaches the end of the domain. Finally, a case with $b = 1$ fails to propagate, reaching distances from the ignition end of $20\delta_T$ in times as long as $t \simeq 6.5$. In this simulation, due to the larger value of b, the flame is extinguished before reaching the end of the domain leaving almost 90% of the fuel unburnt.

3.2. Closed-open propagation

On the contrary, premixed flames ignited at the closed end, $x_0 = 0.99L$, produce a stabilizing overpressure behind the flame. It can be noted that the burnt gases trapped between the flame and the end wall act as a volume source, pushing the reaction region towards the venting end and shortening the burning time. Analogously to the OC configuration, the CO propagation cases in absence of gravity are shown in the panels of Fig. 3. The colored isocontours of temperature are shown from left to right at the last time ($t = 1.0$ for $b = 0$,

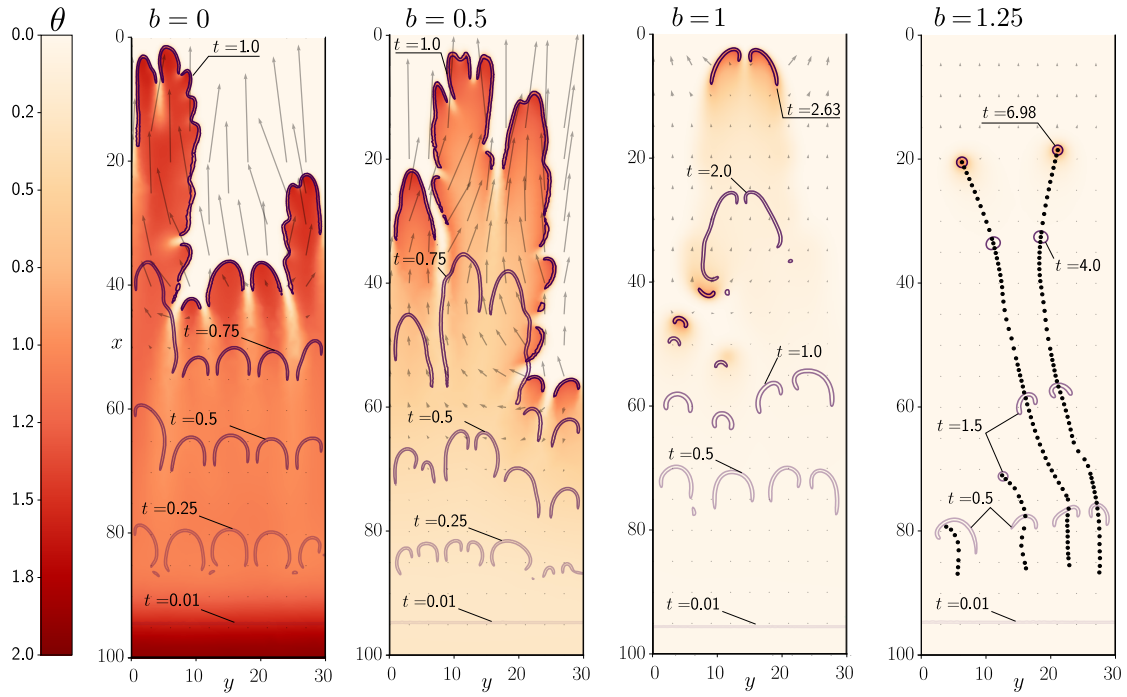

Figure 3: Temperature profiles for flame-front propagation in CO configuration at different times, for increasing values of the heat-loss parameter b and $G = 0$.

$t = 1.0$ for $b = 0.5$, $t = 2.63$ for $b = 1$, and $t = 6.98$ for $b = 1.25$) including dim reaction rate isocontours in previous time steps to illustrate the evolution of the flame in each case.

The adiabatic case ($b = 0$) shows a high degree of symmetry in the y direction during the whole burning process, in contrast with the analogous OC configuration. Moreover, the absence of heat losses yields an important temperature accumulation produced by the burnt gases and the pressure build-up at the closed end. For this reason, more extreme flow velocities are induced in comparison with the OC geometry, while preserving the cell characteristic size. A larger value of $b = 0.5$ produces non-negligible losses which are responsible for further fragmentation of the flame by means of enhanced local extinction, reducing the characteristic cell size and promoting disorder of the front. For $b = 1$, the unstable fragmented flame front evolves to produce isolated flame cells. These circle-like structures arise after traversing half of the domain and interact between them. Later, a stable and symmetrical two-headed cell is developed, which travels steadily towards the end of the chamber. These kind of coupled cells arise naturally for other values of $b \sim \mathcal{O}(1)$. Furthermore, isolated circle-like flames are found for $b = 1.25$, as shown in the rightmost panel of Fig. 3. These small flame cells produce moderate increases of temperature and very low reaction rates. Therefore, small variations are found in the flow field during their propagation. They exhibit a steady behavior remaining active for large periods of time. Finally, these circle-like

flames can be extinguished when heat losses are large enough to overcome the heat released from the flame. In conclusion, isolated cells are more easily restrained and extinguished when acting against the build up of pressure in fresh gases (OC). As expected, a more stable behavior is found for propagation towards an open end where the endurance of weak kernels benefits from piston-like effects (CO).

3.3. Flame velocity and burning times

The qualitative differences shown above between OC and CO configurations are inherent to the imposed boundary conditions and can be characterized with a detailed quantitative post-processing of the numerical data. Major variations are obtained first in the burning time, defined as the period employed by the flame to propagate along the chamber. It depends on the induced base flow that drags out or pushes forward the front. The burning time can be used together with the associated chamber length to represent an average flame velocity in a fixed reference frame. However, the evolution with time of the dimensionless region occupied by the unburnt gases $V_u = \int_\Gamma \mathrm{d}\sigma/(LW)$, with Γ defined as the region in which the mass fraction satisfies the condition $Y > 0.95$, is represented in Fig. 4(a) for OC and Fig. 4(b) for CO configurations under different values of the parameter of heat loss. A monotonic behavior is maintained for the depletion of unburnt reactants for both cases, increasing the burning time as the flame is slowed-down with greater heat losses. The time of complete depletion is significantly shorter for any value of b in the CO case than in the OC case. This is due to the effect of the overpressure that is produced by the confined products. In addition, the expanding flow exiting the chamber produces an exhaust of pure mixture out of the computational domain. Furthermore, the overall propagation rate S_T relative to the planar flame velocity S_L [30] is calculated as

$$\frac{S_T}{S_L} = \frac{1}{LW} \int_0^W \int_0^L \Omega \, \mathrm{d}x\mathrm{d}y. \tag{30}$$

The evolution with time of the propagation rate is plotted in Fig. 4(c) for the OC propagation. Note that a plateau of nearly constant reaction rate and steady propagation is always reached. Nevertheless, for small values of b, this plateau is followed by a sharp decrease to zero once the flame front has consumed the available volume of reactants V_u. For greater values of the heat-loss parameter, this sudden decrease arises as the reaction reaches the end of the chamber ($b = 0.75$ at $t \simeq 6.5$) or extinguishes ($b = 1$ at $t \simeq 7$), leaving a nearly-entire domain of unburnt reactants behind. In the CO case shown in Fig. 4(d), an accelerated propagation takes place thanks to the progressive increase of pressure and temperatures in the gas products located between the flame and the wall. The flame velocity peaks at the point where the amount of unburnt reactants is almost depleted reaching the end of the chamber, and then it progressively diminishes while consuming the available mixture left. For sufficiently large heat losses, the flame extinguishes completely at a finite distance from the ignition point in which the integral of the reaction rate becomes null $S_T = 0$ ($b = 1.25$).

Finally, the x location of the most advanced position of the flame x_f is evaluated at each time instant by direct measurement of the flow variables. This particular value is used to

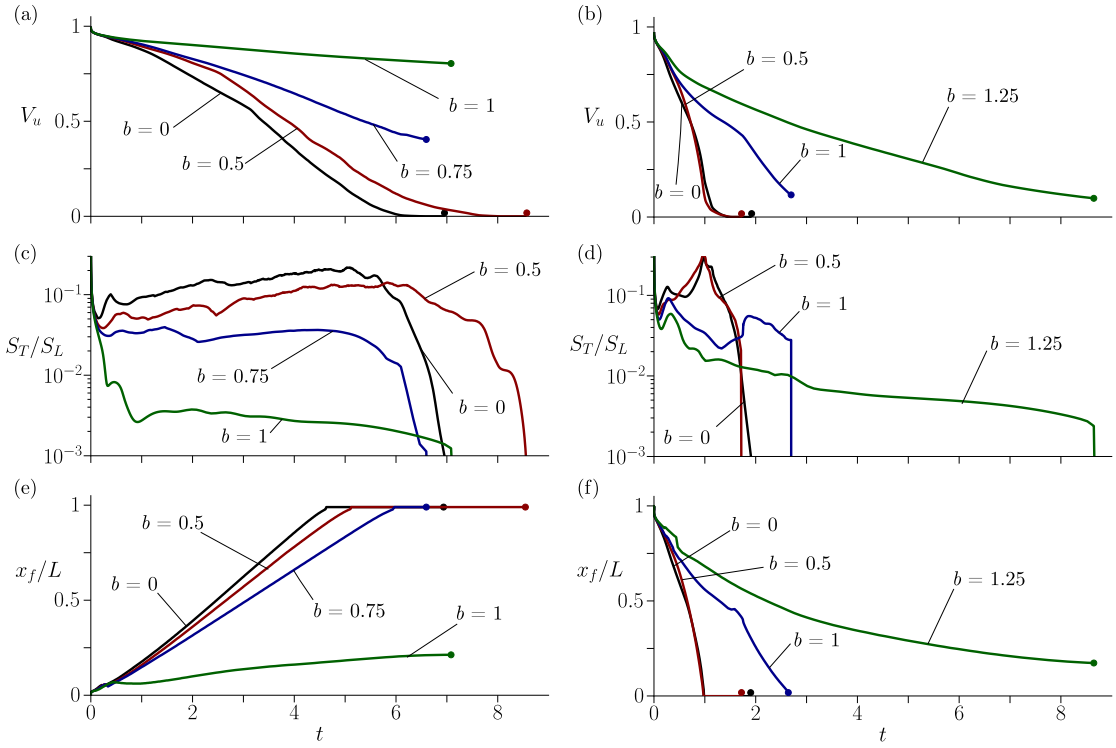

Figure 4: Unburnt volume V_u (a-b), flame velocity S_T/S_L (c-d), and the most advanced position of the flame front x_f/L (e-f) with $G = 0$ and different values of the heat-loss coefficient b in the open-closed (left plots) and closed-open (right plots) configurations. The solid dots indicate $S_T = 0$.

detect the arrival of the front at the end of the chamber. Note that, for OC propagation in Fig. 4(e), ignition is located at the open end in $x \simeq 0$, and reaches the end of the chamber at $x_f/L = 1$. There, the most advanced point of the flame arrives before the full consumption of the reactants has taken place. This effect is also present although less noticeable for the CO configuration Fig. 4(f) with ignition at $x \simeq L$.

3.4. The role of thermo-diffusive instabilities.

The Lewis number considered in our computations is significantly below unity ($Le = 0.3$), as representative of fuels such as hydrogen. Therefore, thermo-diffusive instabilities are likely to heavily affect the development of the flame morphology illustrated in Figs. 2 and 3. To check to what extent this instability intervenes in the formation of circle or comet-like flames, we plot in Fig. 5 the reaction isocontours in OC configuration with $G = 0$ and $Le = 1$. When the Lewis number is chosen to be of order unity, the flame becomes stable regarding thermo-diffusive instabilities and the density jump across the reactive front becomes the only source of instability. In this case, only the perturbations with long wavelength $\Lambda \sim \mathcal{O}(W)$ grow in time, reducing the curvature of the flame that adopts a mushroom-like shape in

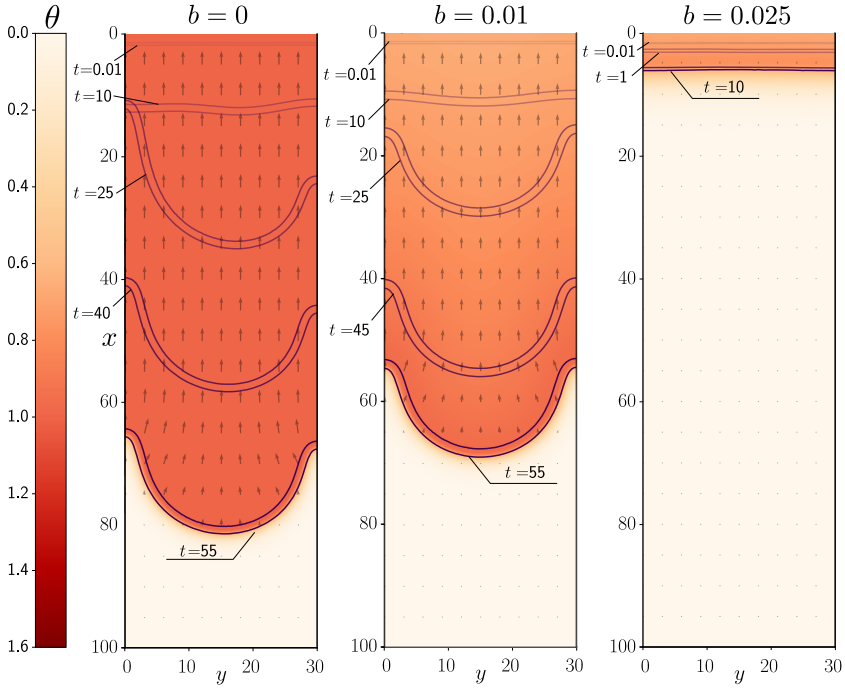

Figure 5: Reaction front evolution in gravity-less OC configuration with $Le = 1$ for increasing values of the heat-loss parameter b. Burning times are $t = 67.5$ for $b = 0$ and $t = 78.6$ for $b = 0.01$. Flame extinction is found for $b > 0.01$.

which heat losses soon offset heat production reducing rapidly the flame temperature and propagation velocity. As expected, the flame shape is left unperturbed until heat losses are sufficiently intense to induce complete extinction with $b \simeq 0.025$. Analogous results where the thermo-diffusive cellular behavior is also hindered are found for $Le > 1$, and are not included in this manuscript. However, in low-Lewis number flames, the front perturbations of small wavelength $\Lambda \sim \mathcal{O}(\delta_T)$ are unstable and produce flame cells with a characteristic size of the order of the flame thickness. Inside those cells, the large curvature of the flame balances heat production and heat losses. This effect upholds high temperatures that keep the reaction going, even when heat losses are relatively large. Under these conditions, the flame approaches extinction at values of the heat loss parameter $b \simeq \mathcal{O}(1)$, much larger than the extinction values of b found for $Le \gtrsim 1$.

4. Heat-loss effects in buoyant flames

Although it has been shown that conductive heat losses play a key role in the appearance of the circle and comet-like flames in lean highly-diffusive mixtures, the transmission of burning kernels can be enhanced or subdued by means of other mechanisms, such as gravity.

In the absence of buoyant convection, heat losses break the reaction front into one or two-headed isolated flame cells that remind the process of flame fragmentation observed in spherical flames [29, 31]. In this section, we will study the effect of gravity on the propagation of flames affected by heat losses.

4.1. Upward propagating flames

We shall first consider the light hot combustion products to be located under the cold mixture. This favors the development of the well-known Rayleigh–Taylor instability. In the first approximation, the flame propagation velocity equals the rising velocity of a bubble with equivalent temperature in adiabatic tubes and channels [32]. Nevertheless, the flow in the hot gas behind the flame is far more complex than the cold gas behind an ascending bubble [33], where a recirculating region behind the front could trigger an unstable behavior of the hot fluid. Heat losses and gravity effects were considered by [10] in a Hele–Shaw cell using infinitely-fast chemistry to conclude that the effect of the Darrieus–Landau instability is reduced due to the attenuation of the density change across the reaction front provided by heat losses. However, the influence of the Lewis number was not considered by the authors.

Notice that, using the reference system defined above in Fig. 1, $G < 0$ in the OC configuration and $G > 0$ in the CO configuration represent flames propagating against gravity. As it can be seen in Figs. 6 and 7, marked differences were observed between the dynamics of flames propagating in the OC or CO configurations.

4.1.1. Open-closed propagation

In this case, the propagation and the structure of the flame does not change significantly for moderate values of the heat loss parameter ($b = 0.5$ or 1). However, the overall propagation rate S_T is evidently affected by heat losses; see the evolution with time of S_T/S_L together with both the unburned volume V_u and the most advanced position of the flame x_f in Fig. 7(a,c,e). Local flame quenching is induced at the flame troughs as the heat loss parameter increases above $b > 0.75$. Then, the flame breaks into several circle-like flame cells separated from each other that travel towards the closed end of the chamber. For $b > 1$, the flame dynamics are modified and the cells formed shortly after ignition become unstable. The surviving one-headed celld grow to reach a maximum size before dividing into two smaller cells. These two interact and either extinguish or grow before splitting again. The dynamics of the new-born cells is erratic with continuous changes of direction and velocity due to the interplay between buoyancy and upstream overpressure. The evolution is shown in Fig. 6(a) for $b = 1.75$, where the path followed by the flame cells is marked with a solid gray line that becomes thicker as the instantaneous velocity of the flame increases. During the final stage ($t = 10$), the maximum temperature computed is $\theta_{max} = 1.15$. Gravity induces a preferential propagation upwards with several branches that arise at splitting events, which form a tree-like structure (Supplementary material, video 1).

The propagation rate shown in Fig. 7(c) changes suddenly after every cell splitting episode. The comet-like flame grows in size cyclically, reducing the maximum temperature of the region and the propagation rate. Minimum values of S_T are reached just before the flame splits into two smaller cells. Then, curvature causes a new temperature increase

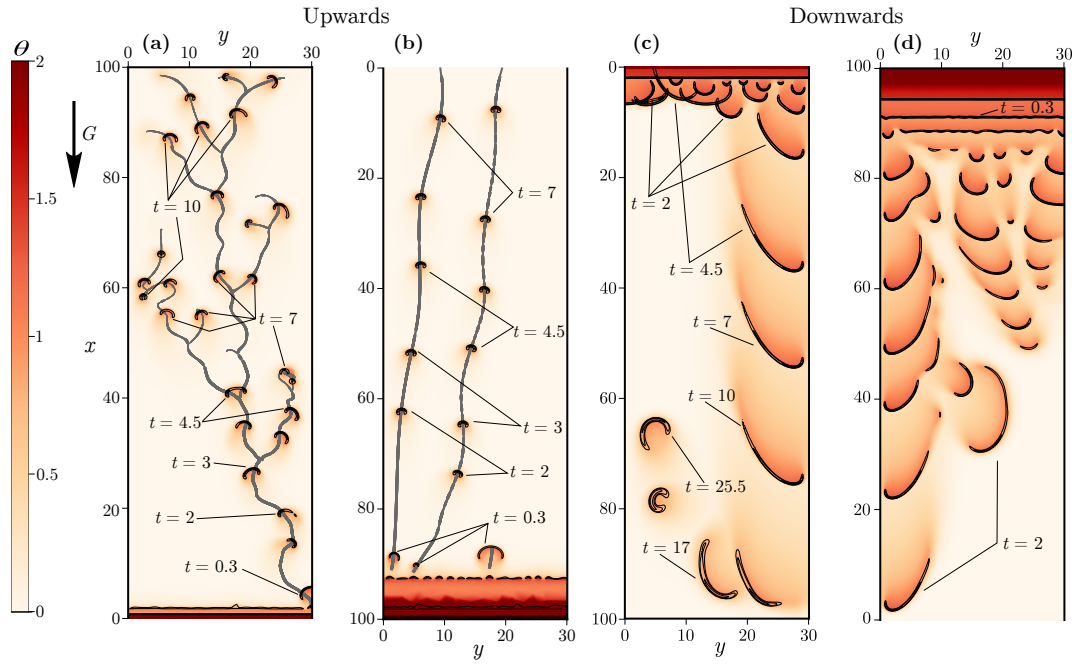

Figure 6: Temperature θ (colored isocontours) and reaction rate Ω (black contours) of flame cells propagating upwards (a) {OC, $G = -10$, $b = 1.75$}, (b) {CO, $G = 10$, $b = 2$}, and downwards (c) {OC, $G = 10$, $b = 0.3$}, (d) {CO, $G = -10$, $b = 0.5$}. The thick lines in (a) and (b) indicate the trajectories followed by the flame cells.

and larger values of S_T, which reaches a local maximum when the cell size is minimum. The small values of S_T explain the long burning times observed in Fig. 7. For moderately large values of the heat losses parameter ($b < 2$), the flame cells only disappear when they reach the end of the chamber leaving, eventually, some amount of fuel unburned. Total flame extinction occurs abruptly close to the ignition region for values of the heat loss parameter $b \gtrsim 2$.

4.1.2. Closed-open propagation

The evolution of V_u, S_T and x_f with time is depicted in Fig. 7(b,d,f) for different values of b. The effect of heat losses is similar to that described above for $G = 0$, with isolated one or two-headed flames cells formed only for $b > 1$ and propagating unsteadily towards the end of the chamber with burning times much shorter than in the OC case. Little or no effect, besides the deceleration of the reaction rate, is observed for smaller values of the heat-loss parameter $b < 1$. Even though eventual flame cell splitting is observed for $b = 1.5$, the isolated flame cells are much more stable than those computed in the OC configuration, given that buoyancy and overpressure effects are complementary here.

A representative example of the stable cell propagation is plotted in Fig. 6(b) for $b = 2$

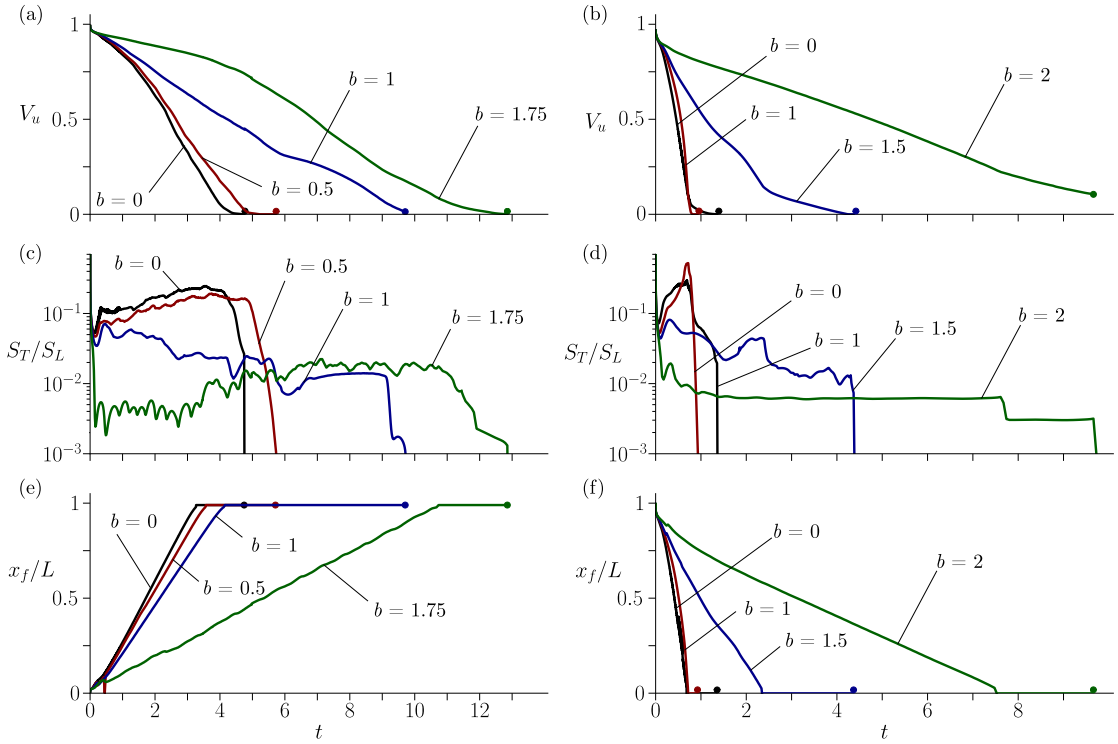

Figure 7: (a-b) burned area V_f, (c-d) flame velocity S_T/S_L and (d-e) the most advanced position of the flame front x_f/L for upward propagating flames with different values of the heat losses coefficient b, in OC (left plots $G = -10$) and CO (right plots $G = 10$) configurations.

and $G = 10$ (Supplementary material, video 2). Once the circle-like flames are formed, they steadily burn small amounts of fuel keeping its size constant, with maximum temperatures such as $\theta_{max} = 1.1$ at $t = 7.54$. The paths are represented as in the previous case, the thickness of the line represents the instantaneous velocity of the flame, which remains almost constant during the whole propagation process. In unconfined near-limit mixtures, flames adopt almost spherical shapes [34] and constitute an ensemble of isolated flame balls. Here, the two circle-like flames that appear after the fragmentation of the reactive front move as a whole, keeping the distance between them.

The burning velocity remains small of the order of $S_T/S_L \simeq 6 \times 10^{-3}$. Finally, one of the flames exits the domain and the overall burning velocity is suddenly divided by a factor of two $S_T/S_L \simeq 3 \times 10^{-3}$ at $t \simeq 7.58$, proving the similarity of the two flame circles. As in the unconfined case described by [16], both flame cells move independently to each other with equal traveling velocities $|d\vec{x}_{cg}/dt| \simeq 10$, where $\vec{x}_{cg}$ is the instantaneous location of the geometric center of the reaction front, a curve defined as the locus of $Y = 0.1$. The stable behavior is explained as both intervening mechanisms, overpressure and buoyancy, act in

the same direction pushing further the extinction event caused by greater heat losses.

4.2. Downward-propagating flames

Flame propagation against buoyancy effects in Hele–Shaw chambers has been explored mainly in the study of flame instabilities [12, 35–37]. However, none of the authors considered the effect of conductive heat losses in their studies. Using the reference system defined in Fig. 1, $G > 0$ in the OC configuration and $G < 0$ in the CO configuration represent flames propagating in the same direction than gravity.

The effect of heat losses is similar to that described above in horizontal and upwards propagating flames. Sufficiently intense heat losses will break the flame front leaving just a single comet-like flame in both the OC and CO configuration, as is shown in Fig. 6(c-d). For flames propagating downwards we find total extinction before one fourth of the chamber length for $b = 0.4$ and $b = 0.6$ in the OC and CO configurations, respectively, in contrast with $b = 1.8$ and $b = 2.05$ computed for upward propagating flames. Larger values of b are required for production of circle-like flames. However, buoyancy effects succeed in pulling the flame away from the fresh reactants under weak-burning conditions and enable extinction events. The curves for V_u, S_T and x_f are qualitatively very similar to those shown in Fig. 4 and are not shown in this document for the sake of conciseness.

5. Structure of the one or two-headed cell flames

Canonical reactive problems have been relentlessly pursued in experiments and proposed as object of study for their simplified theoretical treatment and large potential to increase the understanding of the physical processes involved. The most representative cases being the theorized premixed flame balls in a quiescent atmosphere with spherical solution by Zel'dovich [19] and isolated droplet burning [38, 39]. These spherical configurations have been reproduced and studied in non-propagating microgravity conditions, stabilized by radiative losses [40–42], and therefore have been instrumental to provide useful insight into the mechanisms that control the reaction. However, conductive losses at the plates in the integrated transverse direction, facilitate the appearance of new quasi-two-dimensional canonical configurations that propagate in a fresh mixture environment. Details of the flow field for a steadily-propagating flame cell in absence of buoyancy and including conductive heat losses are shown in Fig. 8 over a moving reference frame. The latter is placed at the center of the propagating cell $\vec{x}' = \vec{x} - \vec{x}_{cg}$.

First, a two-headed stable configuration is depicted in Fig. 8(a) with black lines denoting the contour levels of reaction rate plotted over the colored filled contours of temperature. The flow-field velocity is referred to a frame moving with the flame $\vec{U} - d\vec{x}_{cg}/dt$ and depicted with a vector field on top of the mass fraction distribution in Fig. 8(b). This particular flame shape arises after a reacting cell splits to create a symmetrically coupled front in the CO case $b = 1$ shown above in Fig. 3 at $t = 2.63$. This specific configuration propagates in a steady-state manner, stabilized via convection and heat conduction, and particularly showing local extinction, or absence of total merging, in the origin of the moving frame.

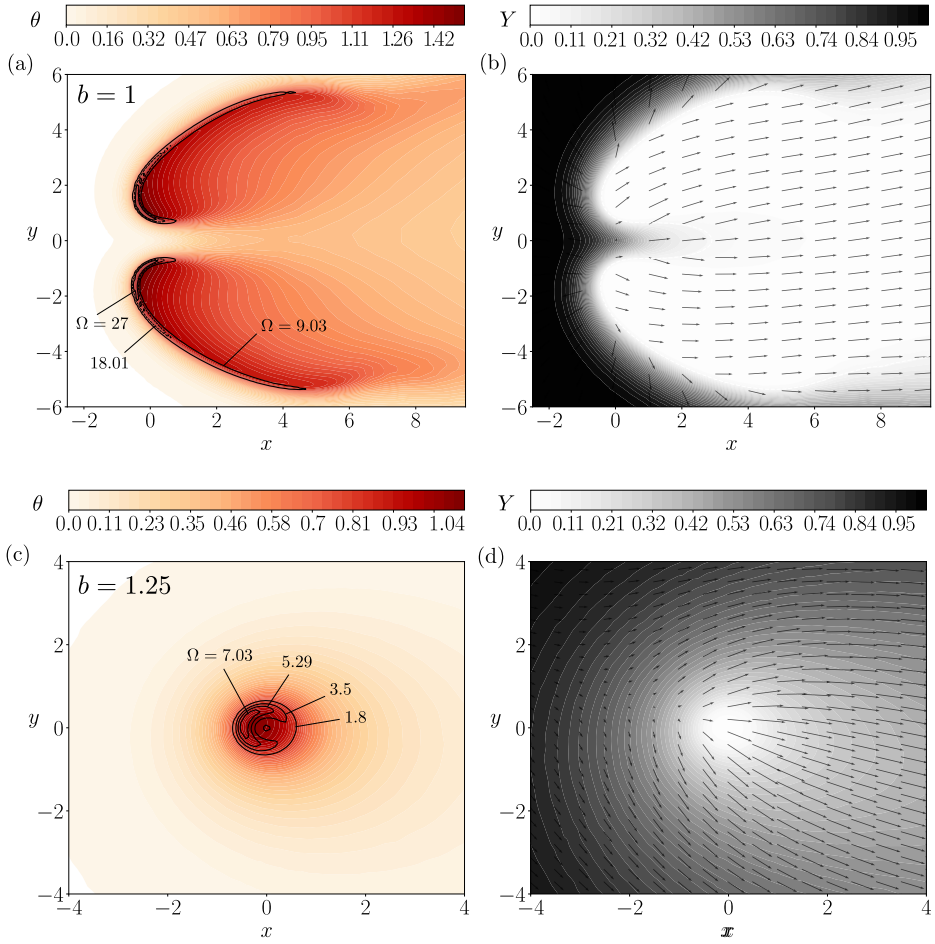

Figure 8: Detail of two-headed (a-b) and semicircular (c-d) flames in moving local axes. Temperature contours and superimposed reaction-rate levels (a-c) and mass-fraction distribution with relative flow field velocity $\vec{v}$ (b-d), are pictured for non-buoyant CO propagation with heat-loss parameter $b = 1$ at time $t = 2.63$ (top) and $b = 1.25$ at $t = 6.98$ (bottom).

In addition, further increase of the heat loss parameter generates a simpler burning front in the form of a circular flame. More precisely, the steady-state propagation of one cellular flame as obtained in the rightmost panel of Fig. 3, with $b = 1.25$ and CO configuration, is shown at $t = 6.98$ in Fig. 8(c) with the respective temperature and reaction rate profiles. The highly-diffusive species considered here ($Le = 0.3$) play a major part in the development of the circular shape. As can be seen in Fig. 8(d), the contour lines of unburned mixture close around the burning cell while the flow field runs parallel to the x axis. This suggests that diffusive transport acts preferentially in the transverse direction and the diffusion of fresh species fills up the trail of depleted reactants behind the burning front. Consequently,

the cell advancing motion is slow enough to enable species diffusion at distances of the order of the flame radius r_f during the local residence time $t_r \sim r_f/\dot{x}_f$ and produce a closed circular burning front. The estimate of the cell velocity $\dot{x}_{cg} \sim 10S_L$ is extracted from Fig. 4(f), where the flame reaches around 80% of the chamber length in $t \sim 8$. In turn, the time of species diffusion is given by $t_d \sim r_f^2/D' \sim Le(r_f^2/D'_T)$. Therefore, flame circles appear for comparable diffusive and residence times $t_r \sim t_d$, which implies that $r_f \sim (10Le)^{-1}(D'_T/S_L) \sim \delta_T/(10Le)$. This is the case of the computations shown in Fig. 8(c) with $Le = 0.3$ and $r_f \sim \delta_T$. However, larger velocities of the cell $\dot{x}_f$, as the case depicted in Fig 8(a) reduce the action of diffusion behind the flame $t_r \ll t_d$, preventing the generation of circular flames.

Furthermore, the relative flow produced by directional fuel consumption produces stabilization by means of heat convection [24]. Nevertheless, heat losses through the plates are essential to the evolution of continuous fronts into these structures, and are responsible for a net reduction of temperature and burning rate, which consequently diminish the relative convection to provide diffusion-reaction equilibrium and steady propagation. This combination of particular diffusive-thermal conditions enables, in a slowly-reacting front, the nearly-circular distribution of isolated reaction.

6. Conclusions

In this work, the propagation of low-Lewis premixed flames in non-adiabatic Hele–Shaw chambers is analyzed. Using the limit $a = h/\delta_T \ll 1$, the three-dimensional configuration simplifies to a quasi-2D problem in which the velocity field is controlled by viscous effects. The resulting system of equations is solved numerically using a finite-element method with an adaptive grid that changes with time to cluster grid elements near the moving reaction front.

We have recalled the widely-known result that steady flame circles cannot exist in a quiescent atmosphere using the reactive-diffusive system written in (1) because of the lack of mathematical solution to the mass fraction profiles. In the adiabatic case ($b = 0$), our results recovered the dynamics of unstable cell growth and the development of diffusive-thermal instabilities found previously in [12]. However, when conductive heat losses are included ($b \neq 0$), our transient numerical calculations have shown the existence of isolated circle or comet-like flame cells travelling along the combustion chamber in the limit of slow propagation velocity. The two-dimensional equivalent to the flame ball arises stabilized by means of conductive heat losses, in comparison to pure convective effects considered by Grcar [24].

The dynamics of the isolated flame cells is very different for horizontal, upward and downward propagating flames. In horizontal chambers ($G = 0$), stable one or two-headed comet-like flames are formed in both OC and CO configurations for moderately large values of b. Both the size of the flame cell and its travelling velocity remain constant. Larger values of the heat loss parameter oblige the flame to adopt a semicircular shape to maintain the temperature high enough to sustain the reaction before total quenching occurs at around $b \simeq 1$.

When propagating in favor of buoyant effects, the dynamic of the isolated flame cells is substantially modified. In the OC configuration, the flame adopts a semicircular shape that undergoes a random walk with several flame-splitting episodes that form alternative paths branching off from a main flame cell pathway that is determined by the buoyancy forces. On the contrary, in the CO configuration, the semicircular flame cells are stable and propagate along the chamber with constant shape and velocity. Larger values of the heat losses parameter ($b \simeq 2$) are necessary to extinguish the flame compared with the non-buoyant case. Finally, for propagation against buoyancy effects, only comet-like stable flames have been observed in our calculations. Values of the extinction heat losses parameter $b \simeq 0.5$ are smaller than upwards propagating flames, and not large enough to enable the generation of the circular regime.

Differential diffusion plays a fundamental role in the formation of both circle or comet-like flames. For mixtures with values of $Le \gtrsim 1$, small flame curvatures develop with important influence of heat losses on the flame temperature. Even for small values of $b \sim 0.025$, heat losses offset heat production inducing a rapid temperature decrease that extinguishes the nearly planar flame. It is only the combined effects of heat losses and differential diffusion what make possible the development of the singular flame structures studied in this paper.

In conclusion, it remains open to report the experimental existence of confined circular stable flames in the limit of highly-diffusive mixtures and low reaction rates provided by moderate heat losses. However, important details on the dynamics of the front are here provided to conduct specific tests in the most likely configurations.

7. Acknowledgements

This work was supported by the project ENE2015-65852-C2-1-R (FV,MSS,DMR) and ENE2015-65852-C2-2-R (DFG,VK) (MINECO/FEDER, UE). Daniel Martínez-Ruiz would like to thank Amable Liñán for fruitful discussions.

Appendix A. Numerical method

Characterization of the flame and flow evolution in relation to the parameters of the problem is performed through CFD simulations. Finite elements are used with an in-house *Freefem*$^{++}$ code to compute numerically the propagation of premixed flames for different conductive heat-losses. The system of equations is solved in the spatial domain Σ, discretized using a conforming triangulation T_h^n, with the subscript h indicating the mesh discretization and n the time instant. The spatial triangulation T_h^n may change from one time step to another, adapting the distribution of grid elements to the evolving features of the numerical solution as shown in Fig. A.9. The element refinement follows a combined criteria that is based on the steepness of the gradient of the temperature θ, reaction rate Ω and pressure p.

The equations are computed in their weak formulation, reducing the calculation to finding the functions $\theta_0(\vec{x},t), Y_0(\vec{x},t)$ and $p_0(\vec{x},t)$, with $\vec{x}$ in a functional space $P_{m,h}$. Here, $P_{m,h}$ constitutes the finite-element space of polynomials of degree m on each cell of the domain triangulation T_h^n. The finite element solution is then expressed as a linear combination of

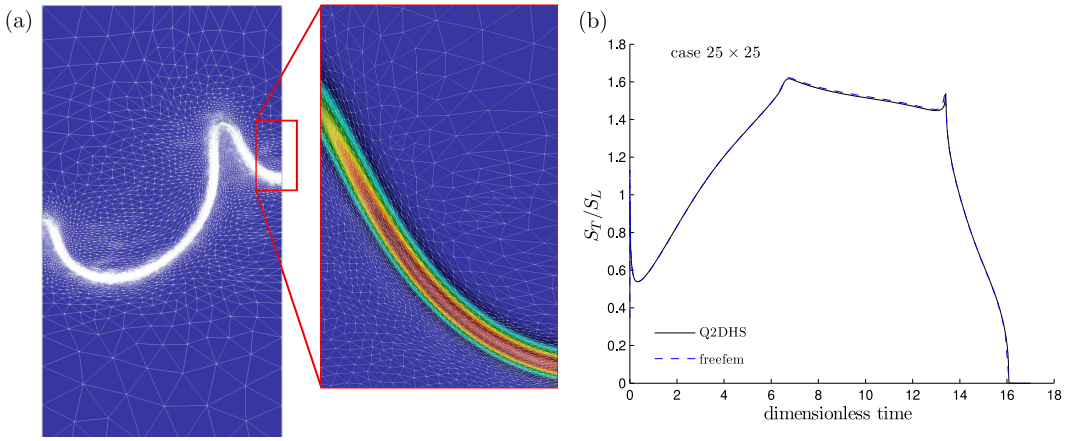

Figure A.9: **(a)** Mesh triangulation for a propagating flame from an open end (top) towards a close end (bottom) at an intermediate time step and zoom-in detail of the region marked with a rectangle. The color map depicts the refinement intensity based on the reaction rate. **(b)** Comparison of the propagation rate between the in-house finite difference code (Q2DHS) used in [12] and the FEM method used herein (b).

basic functions of the functional space $P_{m,h}$, with piece-wise quadratic functions $m = 2$ for θ_0, Y_0, and linear piece-wise polynomials $m = 1$ for pressure p_0 in order to satisfy the inf-sup (or Babuska-Brezzi) condition [27].

A second-order backward difference formula (BDF scheme) is applied for time discretization. At each time step, the values of the dependent variables (namely θ_0, Y_0, and p_0) must be determined. To compute these values, the strongly coupled, highly-nonlinear equations are solved by means of a fully-implicit Newton iterative method. At time t^n, the iteration starts with $k = 1$ using U_x^{n-1} and U_y^{n-1} to solve the system (18), (25), (26) for $\rho_0^{k,n}$, $\theta_0^{k,n}$ and $Y_0^{k,n}$. New values of the pressure variable are obtained $p_0^{k,n}$ by integrating (27), to then obtain the new velocity components $U_x^{k,n}$ and $U_y^{k,n}$ from (21). The procedure continues iteratively until the error

$$\varepsilon = \sum_{j=1}^{3} \frac{||c_j^{k+1,n} - c_j^{k,n}||_\infty}{||c_j^{k+1,n}||_\infty}, c = \rho, \theta, p$$

is smaller than a prescribed tolerance $\varepsilon = 1e - 4$.

Appendix A.1. Maximum size of the mesh elements

The high-resolution of the triangulated mesh used in the computations is a key parameter in determining the accuracy of the results. As indicated above, it is adapted at every time step to cluster elements in the reaction region where the maximum gradients of temperature, reaction rate and pressure are found. Figure. A.9(a) shows a distribution of the triangular

elements at an intermediate instant of the premixed-flame simulation, with an inset that represents in detail the isocontours of reaction rate and the associated locally-adapted mesh. In a typical calculation of a domain $L' = 100\delta_T$, $W' = 30\delta_T$, around $\mathcal{O}(10^5)$ triangular elements and grid points are used, with a minimum element size $h = 0.01$ around the reaction region. Spurious mesh-induced flame oscillations in the edges of the flame have been observed when the grid is sufficiently coarse far from the reaction region. In this case, the pressure field is not properly solved and numerically-induced oscillations are transferred to both the velocity and the mass fraction field. To avoid them, we have introduced an additional pressure-based mesh refinement criteria that ensures the correct calculations of the velocity field that limits the maximum size h_{max} of the grid elements near the open exit of the Hele-Shaw chamber.

Appendix A.2. Numerical test

Bearing in mind the necessity of proving the independence of the numerical method, we have compared the solution obtained using the finite-element code described above with an in-house, time-dependent, second-order finite-difference code (Q2DHS) [12]. This code runs at every time step the aggregation-based algebraic multigrid method [43] to solve the Poisson equation (27). The test case considered here is a squared Hele-Shaw chamber with $L = W = 25$ and an ignition kernel at $(x_0, y_0) = (0, 12.5)$ given by

$$\theta = \theta_i \exp\left(-\left[(x-x_0)^2 + (y-y_0)^2\right]^{1/2}/r_0\right) \tag{A.1}$$

with the ignition end open to the atmosphere and the flame propagating towards the closed end. To compare both codes, we plot in Fig. A.9(b) the propagation rate as defined in (30). The results are indistinguishable, with a maximum deviation error less than 0.6%. Unlike the Q2DHS code, the finite-element code used in our computations introduces the additional complexity of dynamically clustering elements near the reaction front. This complication is offset with an optimization of the computational resources that speeds up the calculations and increases the accuracy of the simulations near the corrugated flame, aspect that turns out to be of utmost importance in the description of the traveling flame cells reported above.

References

[1] M. Matalon, Flame dynamics, Proceedings of the Combustion Institute 32 (1) (2009) 57–82.

[2] M. Sánchez-Sanz, D. Fernández-Galisteo, V. Kurdyumov, Combust. Flame 161 (2014) 1282–1293.

[3] G. Searby, Acoustic instability in premixed flames, Combustion Science and Technology 81 (4-6) (1992) 221–231.

[4] M. Sánchez-Sanz, Premixed flame extinction in narrow channels with and without heat recirculation, Combust. Flame 159 (2012) 3158–3167.

[5] D. Fernández-Galisteo, C. Jiménez, M. Sánchez-Sanz, V. N. Kurdyumov, Effects of stoichiometry on premixed flames propagating in narrow channels: symmetry-breaking bifurcations, Combustion Theory and Modelling 21 (6) (2017) 1050–1065.

[6] K. Bioche, L. Vervisch, G. Ribert, Premixed flame–wall interaction in a narrow channel: impact of wall thermal conductivity and heat losses, Journal of Fluid Mechanics 856 (2018) 5–35.

[7] J. Sharif, M. Abid, P. Ronney, Premixed-gas flame propagation in hele-shaw cells, Spring Technical Meeting joint U.S.Sections, Combustion Institute, Washington D.C. (1999).

[8] K. Maruta, T. Kataoka, N. I. Kim, S. Minaev, R. Fursenko, Characteristics of combustion in a narrow channel with a temperature gradient, Proceedings of the Combustion Institute 30 (2) (2005) 2429–2436.
[9] N. Kim, K. Maruta, A numerical study on propagation of premixed flames in small tube, Combust. Flame 146 (2006) 283–301.
[10] G. Joulin, G. Sivashinsky, Influence of momentum and heat losses on the large-scale stability of quasi-2d premixed flames, Combustion Science and Technology 98 (1-3) (1994) 11–23.
[11] S. Kang, S. Baek, H. Im, Effects of heat and momentum losses on the stability of premixed flames in a narrow channel, Combustion Theory and Modelling 10 (4) (2006) 659–681.
[12] D. Fernández-Galisteo, V. N. Kurdyumov, P. D. Ronney, Analysis of premixed flame propagation between two closely-spaced parallel plates, Combustion and Flame 190 (2018) 133–145.
[13] F. Veiga-López, D. Martínez-Ruiz, E. Fernández-Tarrazo, M. Sánchez-Sanz, Experimental analysis of oscillatory premixed flames in a hele-shaw cell propagating towards a closed end, Combustion and Flame 201 (2019) 1–11.
[14] D. Fernández-Galisteo, V. N. Kurdyumov, Impact of the gravity field on stability of premixed flames propagating between two closely spaced parallel plates 37 (2019) 1937–1943.
[15] L. Schlapbach, Technology: Hydrogen-fuelled vehicles, Nature 460 (7257) (2009) 809.
[16] F. A. Williams, J. F. Grcar, A hypothetical burning-velocity formula for very lean hydrogen–air mixtures, Proceedings of the Combustion Institute 32 (1) (2009) 1351–1357.
[17] J. Yanez, M. Kuznetsov, J. Grune, Flame instability of lean hydrogen–air mixtures in a smooth open-ended vertical channel, Combustion and Flame 162 (7) (2015) 2830–2839.
[18] N. Drozdov, Y. B. Zel'dovich, Diffusion phenomena at the limit of flame propagation: An experimental study of the inhibition of explosive mixtures of carbon monoxide, Zhurnal fizicheskoi khimii 17 (1943) 134–144.
[19] Y. B. Zeldovich, Theory of combustion and gas detonation, Academy of Sciences (USSR), Moscow–Leningrad (1944).
[20] P. D. Ronney, M.-S. Wu, H. G. Pearlman, K. J. Weiland, Experimental study of flame balls in space: Preliminary results from STS-83, AIAA Journal 36 (8) (1998) 1361–1368.
[21] J. Buckmaster, G. Joulin, P. Ronney, The structure and stability of nonadiabatic flame balls, Combustion and Flame 79 (3-4) (1990) 381–392.
[22] J. Buckmaster, G. Joulin, P. Ronney, The structure and stability of nonadiabatic flame balls: II. Effects of far-field losses, Combustion and Flame 84 (3-4) (1991) 411–422.
[23] J. Buckmaster, M. Smooke, V. Giovangigli, Analytical and numerical modeling of flame-balls in hydrogen-air mixtures, Combustion and Flame 94 (1-2) (1993) 113–124.
[24] J. F. Grcar, A new type of steady and stable, laminar, premixed flame in ultra-lean, hydrogen–air combustion, Proceedings of the Combustion Institute 32 (1) (2009) 1011–1018.
[25] Z. Zhou, Y. Shoshin, F. E. Hernández-Pérez, J. A. van Oijen, L. P. de Goey, Formation and stabilization of multiple ball-like flames at earth gravity, Combustion and Flame 192 (2018) 35 – 43.
[26] V. N. Kurdyumov, M. Matalon, Flame acceleration in long narrow open channels, Proceedings of the Combustion Institute 34 (1) (2013) 865–872.
[27] D. Boffi, F. Brezzi, M. Fortin, et al., Mixed finite element methods and applications, Vol. 44, Springer, 2013.
[28] J. Yuan, Y. Ju, C. K. Law, Coupled hydrodynamic and diffusional-thermal instabilities in flame propagation at subunity Lewis numbers, Physics of fluids 17 (7) (2005) 074106.
[29] L. Kagan, S. Minaev, G. Sivashinsky, On self-drifting flame balls, Mathematics and Computers in Simulation 65 (4-5) (2004) 511–520.
[30] J. Daou, M. Matalon, Influence of conductive heat-losses on the propagation of premixed flames in channels, Combustion and Flame 128 (4) (2002) 321–339.
[31] L. Kagan, G. Sivashinsky, Self-fragmentation of nonadiabatic cellular flames, Combustion and flame 108 (1-2) (1997) 220–226.
[32] Y. Shtemler, G. Sivashinsky, On upward propagating flames, Combustion science and technology 102 (1-6) (1994) 81–93.

[33] F. Higuera, Numerical simulation of the upward propagation of a flame in a vertical tube filled with a very lean mixture, Combustion and Flame 158 (5) (2011) 885–892.
[34] Y. Shoshin, J. Van Oijen, A. Sepman, L. De Goey, Experimental and computational study of the transition to the flame ball regime at normal gravity, Proceedings of the Combustion Institute 33 (1) (2011) 1211–1218.
[35] C. Almarcha, J. Quinard, B. Denet, E. Al-Sarraf, J. Laugier, E. Villermaux, Experimental two dimensional cellular flames, Physics of Fluids 27 (9) (2015) 091110.
[36] E. Al Sarraf, C. Almarcha, J. Quinard, B. Radisson, B. Denet, Quantitative analysis of flame instabilities in a Hele-Shaw burner, Flow, Turbulence and Combustion 101 (3) (2018) 851–868.
[37] E. Al Sarraf, C. Almarcha, J. Quinard, B. Radisson, B. Denet, P. Garcia-Ybarra, Darrieus–Landau instability and Markstein numbers of premixed flames in a Hele-Shaw cell, Proceedings of the Combustion Institute 37 (2) (2019) 1783–1789.
[38] G. Godsave, Burning of fuel droplets, Symposium (international) on combustion 4 (1) (1953) 818–830.
[39] D. Spalding, The combustion of liquid fuels, Symposium (international) on combustion 4 (1) (1953) 847–864.
[40] P. D. Ronney, Understanding combustion processes through microgravity research, Proceedings of the Combustion Institute 27 (2) (1998) 2485–2506.
[41] D. L. Dietrich, J. B. Haggard Jr, F. L. Dryer, V. Nayagam, B. D. Shaw, F. A. Williams, Droplet combustion experiments in spacelab, Symposium (International) on Combustion 26 (1) (1996) 1201–1207.
[42] E. Fernández-Tarrazo, A. L. Sánchez, A. Liñán, F. Williams, The structure of lean hydrogen-air flame balls, Proceedings of the Combustion Institute 33 (1) (2011) 1203–1210.
[43] Y. Notay, AGMG software and documentation, `http://homepages.ulb.ac.be/~ynotay/AGMG`.